Enhanced Morphological Properties of Macroporous Silicon with the Incorporation of Au-Ag Bimetallic Nanoparticles for Improved CO_2 Gas Sensing

Alwan M. Alwan[1] · Muslim F. Jawad[1] · Duaa A. Hashim[1]

Abstract

In this work, the effects of incorporating bare macroporous silicon (macro-Psi) layer with bimetallic nanoparticles Au-Ag on the performance Psi CO_2 gas sensor synthesized by a laser-assisted etching (LAE) process were investigated. Well-controlled and simple immersion process of bare macro-Psi layer in the 10^{-3} M of silver nitrate ($AgNO_3$) and chloroauric acid ($HAuCl_4$) individually and in the mixing solution with ratio 1:1 was employed to synthesize monometallic AuNPs/macro-Psi, AgNPs/macro-Psi, and bimetallic Au-AgNPs/macro-Psi hybrid structures of CO_2 gas sensors. Morphological properties of bare macro-Psi layer, monometallic, and bimetallic hybrid structures were investigated using X-ray diffraction (XRD), field emission scanning electron microscope (FE-SEM), and energy-dispersive X-ray analysis (EDS). Electrical characteristics (I–V) of the sensor were measured primary in a vacuum case and with CO_2 at 0.2, 0.5, 1, and 1.5 mbar gas pressures. The result showed a significant enhancement in sensitivity and temporal response of the bimetallic hybrid structures compared with that of monometallic and bare macro-Psi layer and an enhanced performance of the sensors due to the high value of integrated specific surface area of the bimetallic nanoparticles and the resulting Schottky barrier height.

Keywords Monometallic nanoparticles · Bimetallic nanoparticles · Sensitivity · CO_2 gas sensing · Macro-Psi

Introduction

Psi-based gas sensors for incessant observing of CO_2 in air environment have attracted much attention as an international concern. The improvement of low-cost, steady operation, and high sensitivity room temperature gas sensor is a significant issue [1, 2]. Bare Psi has huge interior specific surface areas up to 600 m^2/cm^3 and extraordinary activities in surface reaction, which consequently improved gas absorptive effects [3]. The incorporation process of Psi layer with monometallic nanoparticles will modify the Psi surface properties and hence enhance the gas-detecting process [4, 5]. Alloy bimetallic of Au and Ag nanoparticles in the field of chemical sensors (optically and electrically based operation) is of significant importance since they have interesting specific surface area and size-dependent electrical, chemical, and optical properties [6–10]. Alloying process of bimetallic nanoparticles will occur due to simultaneous salts in ion reduction

process with silicon dangling bonds, especially when they have identical lattice constants [11]. Naama et al. studied the I–V characteristics and sensing properties of silicon nanowires modified with monometallic platinum and gold nanoparticles as CO_2 sensors, and they found a high dependence of sensing performance on the nanoparticle type [4]. More recently, Alwan et al. prepared meso-PSi/AuNP hybrid structures for CO_2 gas sensor operation at room temperature. They found that the structural aspects (size, shape, and specific surface area) of the Au nanoparticle extremely affect the performance of the hybrid structure [1].

In the current research, synthesis and performance enhancement of modified macro-Psi with monometallic Au, Ag NPs, and bimetallic Au-Ag NP CO_2 gas sensors for room temperature operation were investigated and analyzed.

Experimental Parts

Preparation of Bare Macro-Psi Layer

N-type Si substrate of 10 Ω cm resistivity and (100) orientation was employed in this research. The silicon substrates

✉ Alwan M. Alwan
  alkrzsm@yahoo.com

1 Department of Applied Science, University of Technology, Baghdad, Iraq

were cut into (2×2 cm^2) squares. Earlier to etching, the native SiO$_2$ was detached from the Si substrate by immersing the substrates in dilute 8% HF solution. The rear surface of Si samples was thermally coated with 0.8-μm-thick aluminum layer. The macro-Psi layer was prepared through a laser-assisted etching (LAE) process 24% HF solution via current density of about 20 mA/cm^2 for 20 min with 25 mW/cm^2 and 630-nm laser illumination power density and wavelength, respectively. The setup of etching process is shown in Fig. 1. Later materialization, the bare macro-Psi samples were washed in water and permitted to dry at ambient air.

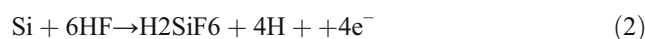## Preparation of Monometallic and Bimetallic Hybrid Structures

Of AgNO$_3$ salt with a purity of 99.99%, 10^{-3} M was dissolved by triply distilled water to prepare an aqueous solution. The HAuCl$_4$·3H$_2$O at a concentration 10^{-3} M was dissolving in the mixture of 3 M from HF and distilled water with volume that is about 20 ml, resulting an aqueous solution. The concentration of the salt solutions (AgNO$_3$ and HAuCl$_4$) was calculated by [12]

$$\text{Molarity} = \frac{\frac{W}{M.Wt}}{V} \tag{1}$$

where W (g) is the weight of the salts, $M.Wt$ (g/mol) is the molecular weight, and V is the volume of the dissolved solution.

Bare macro-Psi layers were immersed individually in the aqueous solution of the AgNO$_3$ and HAuCl$_4$ for 5 and 1 min for Ag and Au, respectively, at room temperature. Bimetallic Au-AgNPs were prepared by simple immersion process of

bare macro-Psi layer in the 10^{-3} M of AgNO$_3$ and HAuCl$_4$ with 1:1 mixing ratio for immersion time of about 2 min. The ion reduction process of Au^{+3} and Ag^{+1} through the dangling bond Si–H of the macro-Psi layer is expressed as follows [1, 12, 13]:

$$Si + 6HF \rightarrow H2SiF6 + 4H + + 4e^- \tag{2}$$

$$Au^{+3} + 3e^- \rightarrow Au \tag{3}$$

$$Ag^{+1} + e^- \rightarrow Ag \tag{4}$$

In order to measure the current–voltage characteristics of bare macro-Psi layer and the incorporating layer with monometallic and bimetallic nanoparticles, two aluminum electrodes were deposited on the back and front side of the substrate. The front electrical electrode above the hybrid structures was made up by depositing a thin aluminum layer. Figure 2 displays a schematic illustration of monometallic AuNPs/macro-Psi, AgNPs/macro-Psi, and bimetallic Au-AgNPs/macro-Psi hybrid structures. Morphological features of bare macro-Psi layer and incorporating with monometallic and bimetallic nanoparticles were investigated using X-ray diffraction (XRD), field emission scanning electron microscope (FE-SEM), and energy-dispersive X-ray analysis (EDS). Bare macro-Psi layer, monometallic, and bimetallic nanoparticle dimensions were assessed by means of special software programs ImageJ type 8. Finally, the hybrid structure gas sensors were placed in a small vacuum-packed cavity with an inlet and outlet facility of gases at pressures of CO$_2$ in the range 0.2, 0.5, 1, and 1.5 mbar. I–V characteristics at forward case were measured using an electrometer Kiethly 6485 and DC power supply Furnall LT30-2.

Results and Discussion

Structural Characterization of Bare Macro-Psi Layer and Hybrid Structures

The XRD characteristic of bare macro-Psi layer after incorporation with monometallic AuNPs, AgNPs, and bimetallic Au-AgNPs is exposed in Fig. 3. Figure 3a, b shows two particular diffraction peaks at 38.4° and 44.6° for AuNPs and 38.18° and 44.18° for AgNPs that match up to (111) and (200) diffraction planes, correspondingly, fitting to the AuNPs and AgNP FCC structure. These results that approve with the ASTM chart statistics are 04-0783 and 04-0784 for Ag and Au, respectively [14, 15]. Figure 3c shows the XRD pattern of bimetallic Au-AgNPs with diffraction peaks at 38.12° and 44°; these peaks are related to the Au and Ag nanoparticles [14]. The XRD peaks of Au-Ag bimetallic nanoparticles are broader than those of monometallic AuNPs and AgNPs. The X-ray diffraction peak of the mixture can be understood to consist of
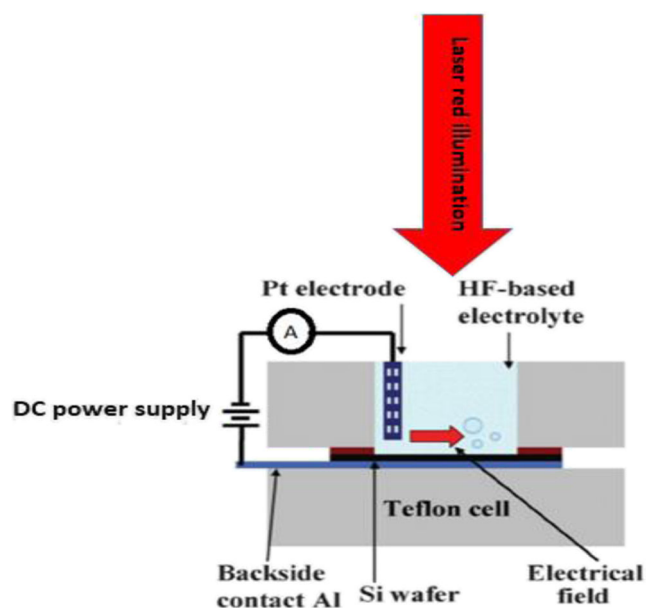

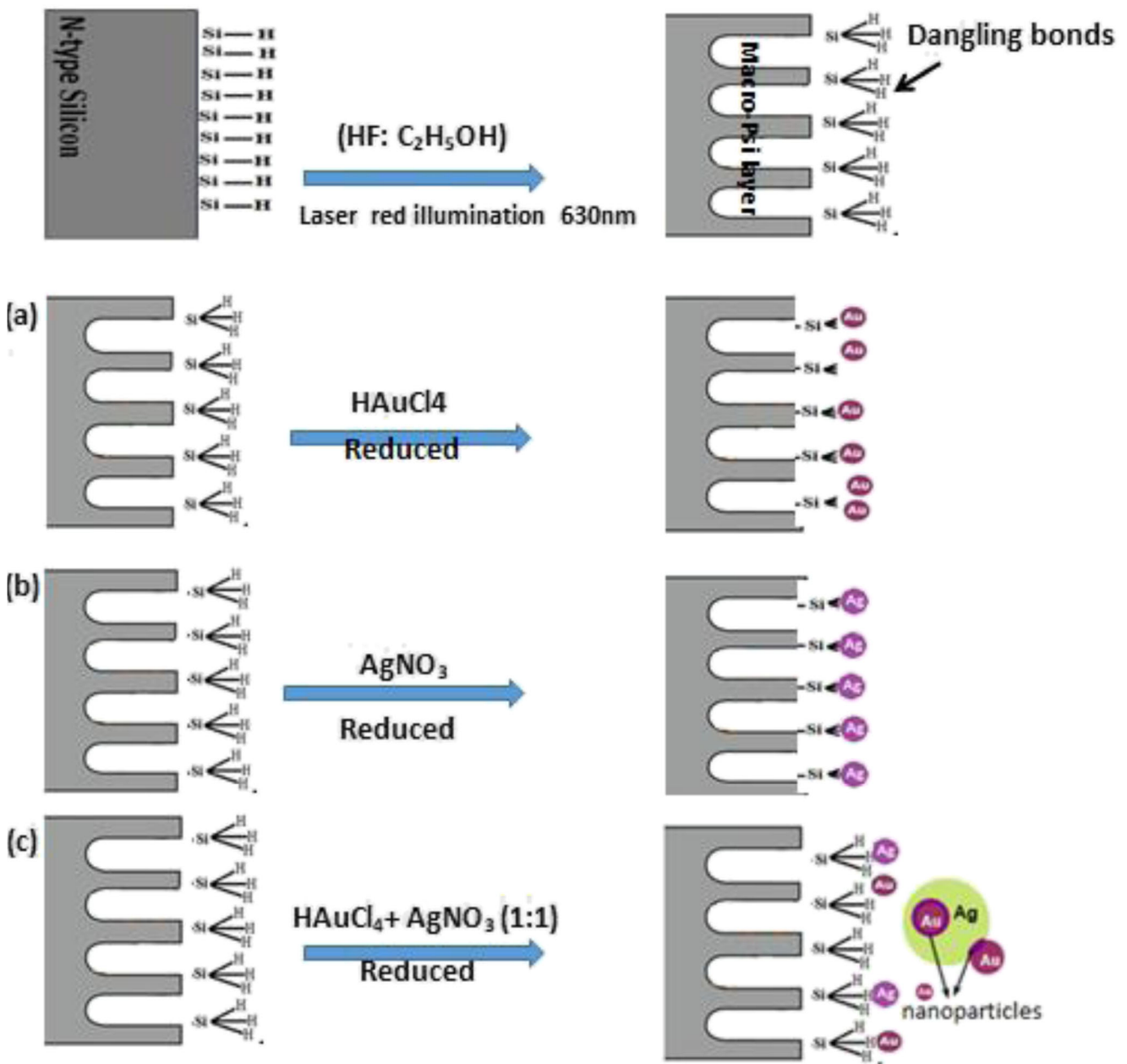
Fig. 1 Preparation setup of bare macro-Psi layer

Fig. 2 Schematic illustration of monometallic **a** AuNPs/macro-Psi, **b** AgNPs/macro-Psi, and **c** bimetallic Au-AgNPs/macro-Psi hybrid structures

the overlap of the diffraction peaks of both slight and large ones, which is consistent with the XRD result in Fig. 3d.

The XRD peaks of AgNPs and therefore its content in the resulting bimetallic nanoparticles are higher than those of AuNPs. This growing of silver element in the alloy may be due to the fact that every silver ion needs only one electron, while gold ions required three electrons to carry out the reduction process [16]. The formation of the bimetallic Au-Ag nanoparticles is based upon the ion reduction of their metal salts which can be strongly owing to identical lattice constants of 0.408° and 0.409A°, correspondingly, for Au and Ag. This slight change in lattice constants being slighter than the

amplitude of thermal vibrations of atoms has already been postulated to favor materialization even at the nanometer scale [14]. The average nanoparticle grain size was calculated by using Scherer's formula [17]

$$L = \frac{0.89 \, \lambda}{B\cos\theta} \tag{5}$$

where L is the nanoparticle grain size in nanometer, 0.89 is the value of the shape factor, λ is the wavelength of the X-ray 1.5406 A°, β is the full-width half-maximum in radian, and Θ is the diffraction angle in degree. The specific surface area
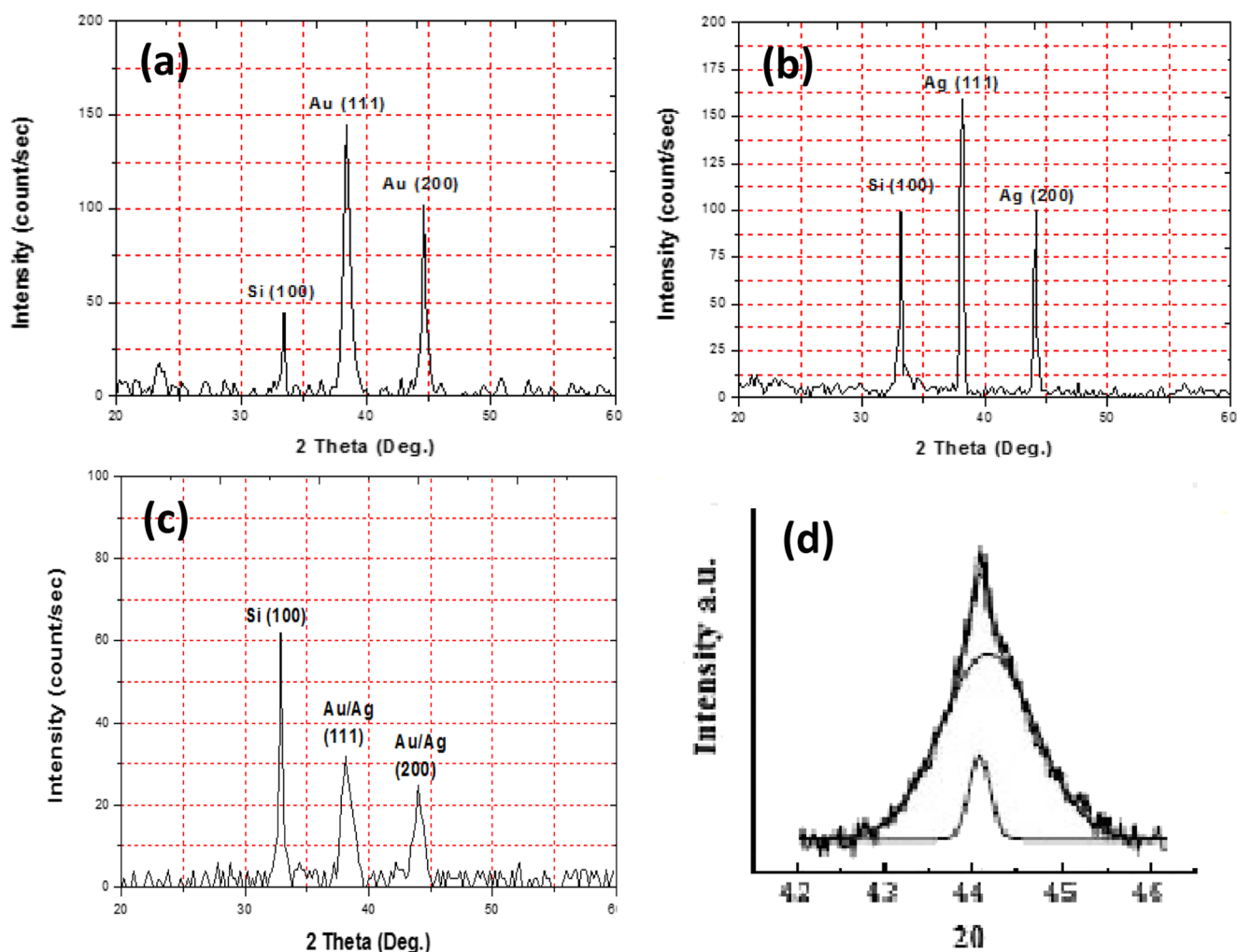
Fig. 3 XRD patterns of **a** AuNPs/macro-Psi, **b** AgNPs/macro-Psi, **c** bimetallic Au-AgNPs/macro-Psi hybrid structures, and **d** peaks overlapping

(S.S.A), one of the figures of merit of the nanostructured material, is given as [18]

$$SSA = \frac{6000}{\text{Nanoparticle grain size} \times \text{density}} \quad (6)$$

The density of monometallic Au and Ag is about (19.3 and 10.5) g/cm^3, respectively, while the density of bimetallic Au-Ag nanoparticles can be calculated by using equation [19]

$$D = \frac{a \times \rho + b \times \rho}{a + b} \quad (7)$$

where D = density of the bimetallic nanoparticles that is about 12.98 g/cm^3 and a = wt% Au and b = wt% Ag that depends on the metal percentages in the EDS analysis. Table 1 demonstrates the nanoparticle grain size and SSA of monometallic Au, Ag, and bimetallic Au-Ag nanoparticles.

Based on Table 1, it can be seen that incorporating of Au-AgNPs leads to enhance the structural characterization of macro-Psi layer by lowering the metallic nanosize and hence

improving SSA compared with that of monometallic Au and Ag nanoparticles.

Figure 4a shows the morphological features of bare macro-Psi layer; the surface contains a pore-like structure with different pore sizes. The images reveal that some pores are overlapping, and the pores are randomly distributed on the porous surface. The pore sizes range from 0.55 to 1.54 μm, and the highest peak at 0.95 μm with percentage 27.5% is shown in

Table 1 Nanoparticle grain size and specific surface area (SSA) of monometallic and bimetallic nanoparticles

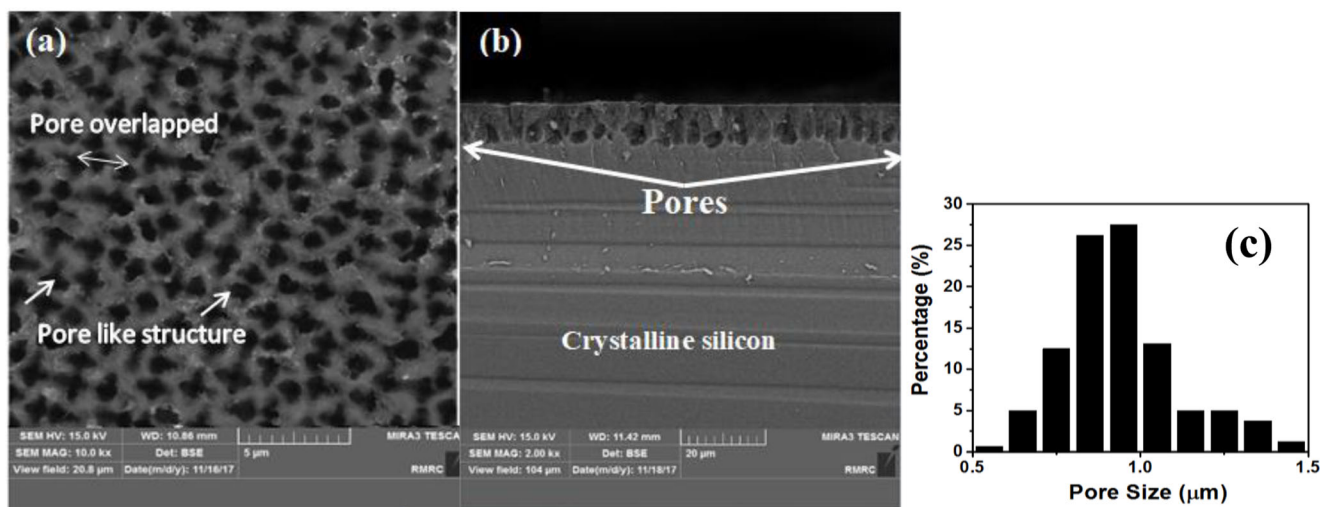| Hybrid structure	Plane (111)		Plane (200)	
	Nanoparticle size (nm)	SSA (m^2/ g)	Nanoparticle size (nm)	SSA (m^2/g)
AuNPs/macro-Psi	21.9	14.2	25.9	12.03
AgNPs/macro-Psi	21.61	26.4	31.3	18.3
Au-AgNPs/macro-Psi	7.98	57.9	9.52	48.56

Fig. 4 FE-SEM images of bare macro-Psi layer **a** surface morphology, **b** cross section of FE-SEM image, and **c** the statistical distribution of pore size of macro-Psi layer

Fig. 4c. The cross section of the FE-SEM image of the macro-Psi layer is shown in Fig. 4b, in which the layer thickness is around 12 μm, and it is easy to differentiate that the pore size varies gradually from the upper porous surface to the bulk interface region. The gravimetrical method [20], implemented to estimate the porosity, revealed around 70% porosity.

Figure 5a shows the FE-SEM images of monometallic AuNPs/macro-Psi hybrid structure; the surface morphology of the growth of AuNPs on the walls of the individual pores follows. The Au nanoaggregates form a land mass of AuNPs over the macro-Psi surface; this is attributed to the enhancement of gold ion reduction process by the high density of the dangling bonds (nucleation sites). The AuNPs were deposited with the distribution in size extending from 35 to 95 nm, and

the peak is about 7.5 nm with percentage 43.75%. The cross section of FE-SEM images of the macro-Psi layer is displayed in Fig. 5b.

Figure 6a shows the FE-SEM images of monometallic AgNPs/macro-Psi hybrid structure; the surface morphology of Ag nanoparticles is mainly deposited on macro-Psi surface in the form of round nanoparticles like fish eggs, and they are dispersed with a double layer of the sample. This morphology may relate to the numerous density of nucleation sites; in addition, every silver ion needs only one electron in the reduction process to nanoparticles, so the high growth rate can be expected for AgNPs. Figure 6b represents an FE-SEM cross section of Ag NPs deposited on macro-Psi layer; it can be seen that the AgNPs enter inside the pores of
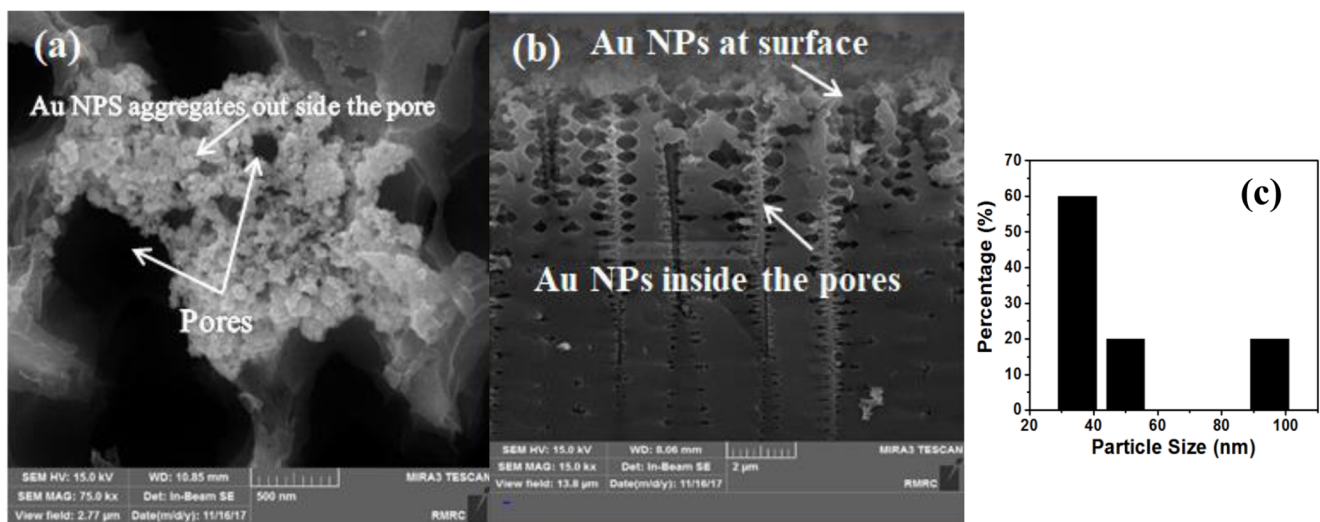

Fig. 5 FE-SEM images of monometallic AuNPs/macro-Psi hybrid structure **a** surface morphology, **b** cross section of FE-SEM image, and **c** the statistical distribution of AuNP sizes deposited on macro-Psi layer
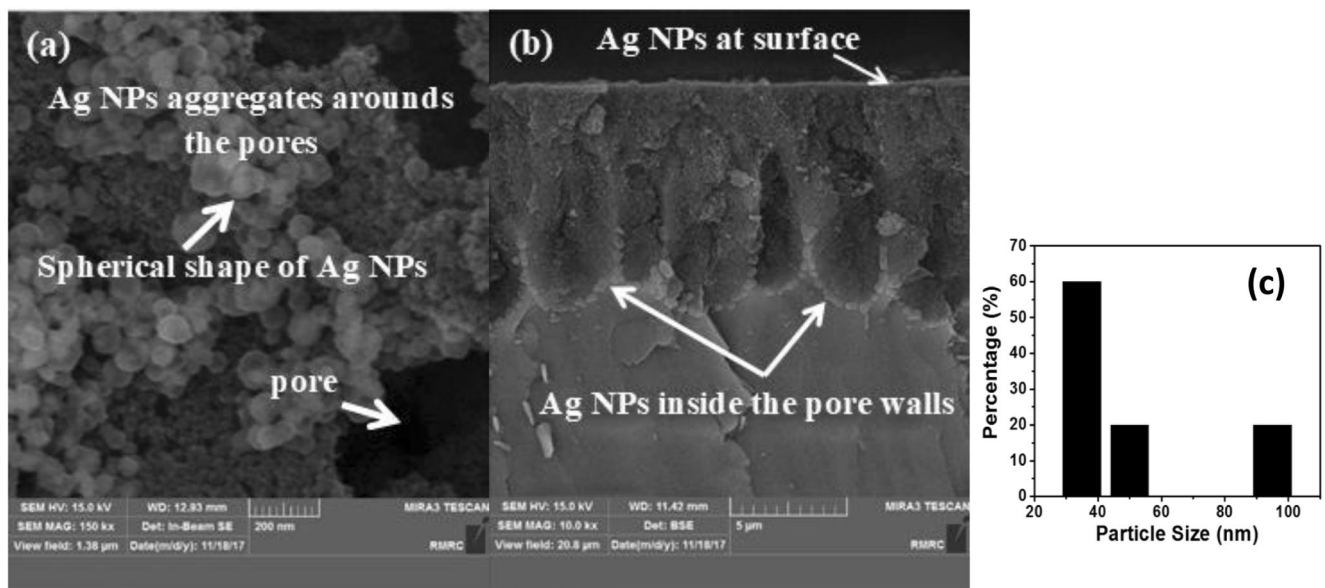
Fig. 6 FE-SEM images of monometallic AgNPs/macro-Psi hybrid structure **a** surface morphology, **b** cross section of FE-SEM image, and **c** the statistical distribution of Ag NP sizes deposited on macro-Psi layer

the macro-Psi layer. The size distribution ranges from 35 to 75 nm, and the peak is about 20 nm with percentage 58.04% as shown in Fig. 6c.

Figure 7a shows the FE-SEM images of bimetallic Au-AgNPs/macro-Psi hybrid structures; the bimetallic Au-AgNPs are mainly composed of high density of uniformly distributed spherical particles that cover the macro-Psi surface. From Fig. 7b, which characterizes FE-SEM cross section of Au-AgNPs deposited on macro-Psi surface, it can be seen that the Au-AgNPs enter inside the pores of the macro-Psi structure. From these figures, it is clear that the monometallic

and bimetallic are positioned outer of the pores in the porous matrix and also come inside the pores. This means that the macro-Psi layer morphology (pore-like structure) provided a high density of appropriate nucleation sites for the nanometallic growth, the size extending from 50 to 950 nm, and the peak is about 50 μm with percentage 43.8% as shown in Fig. 7c.

EDS was used to explore the modification in the surface composition of macro-Psi layer due to the depositing of metallic nanoparticles. Figure 8a–d displays the existence of Au, Ag, Au-Ag, and Si elements of the macro-Psi
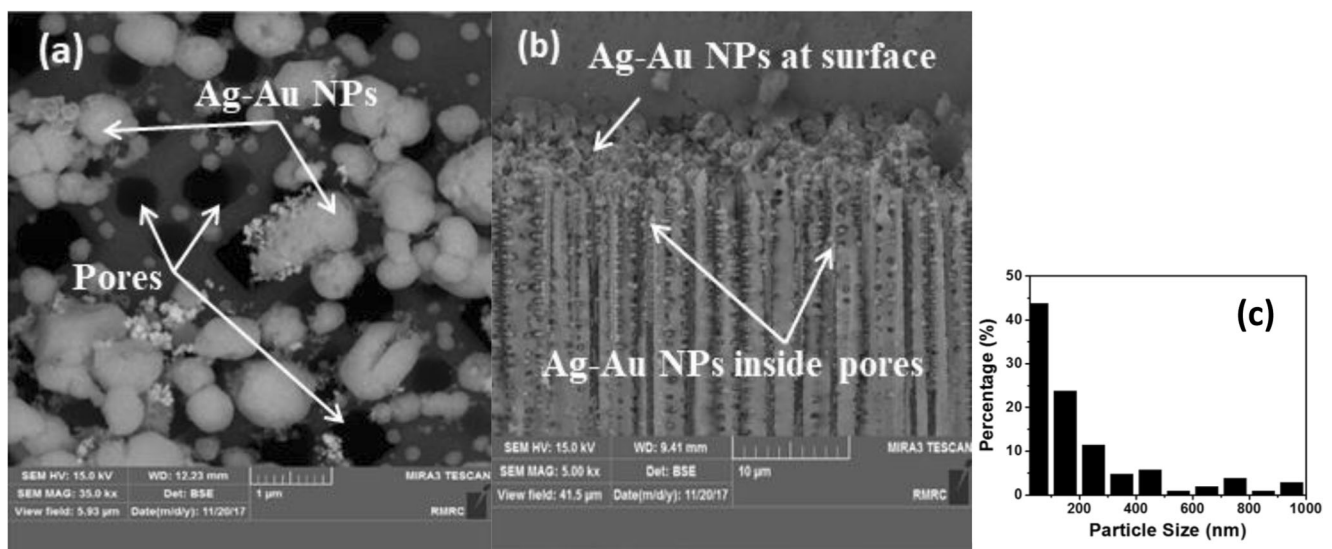

Fig. 7 FE-SEM images of bimetallic Au-AgNPs/macro-Psi hybrid structure **a** surface morphology, **b** cross section of FE-SEM image, and **c** statistical distribution of Au-Ag NP sizes deposited on macro-Psi layer
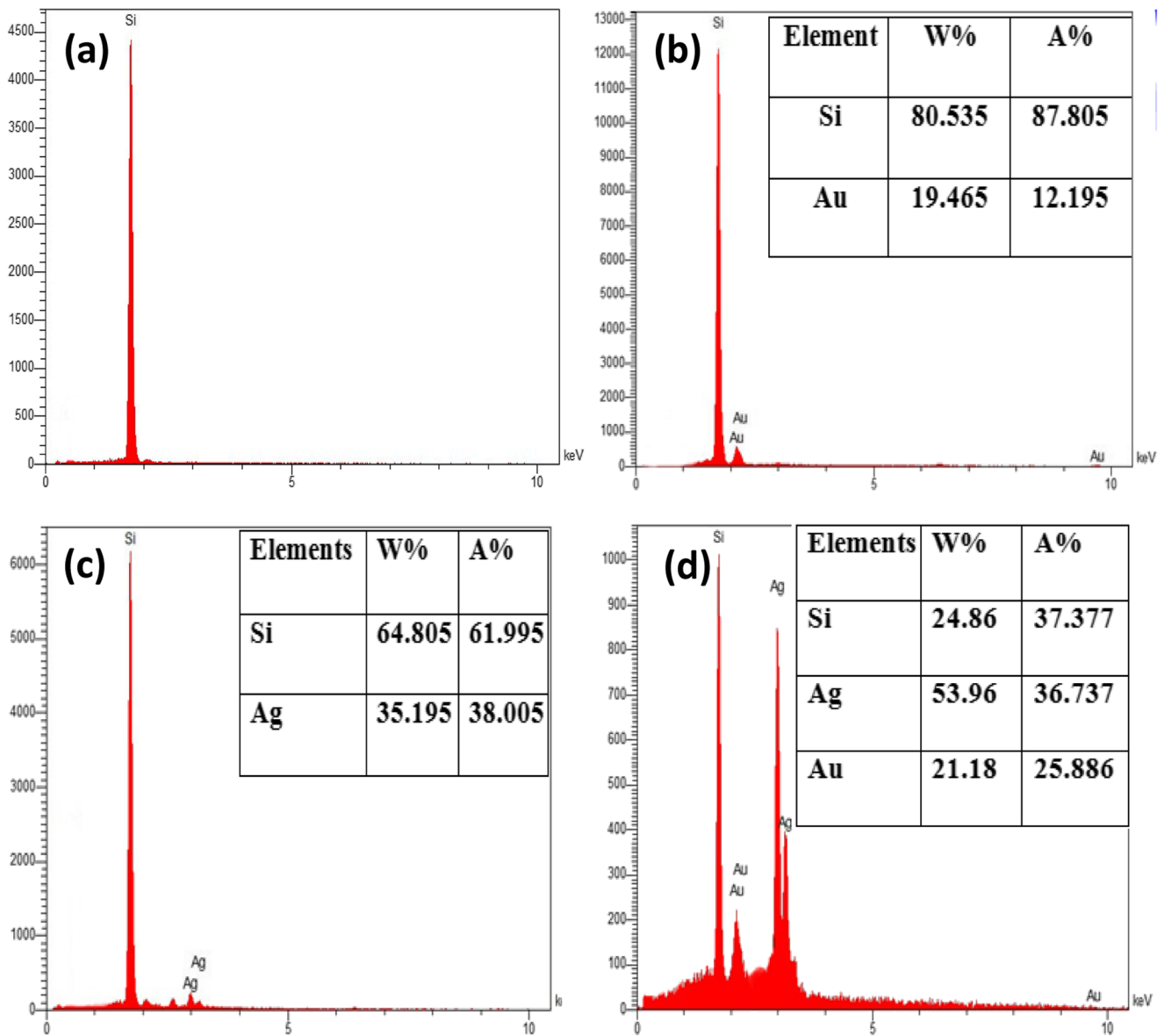
Fig. 8 EDS analysis of **a** bare macro-Psi layer, **b** AuNPs/macro-Psi, **c** AgNPs/macro-Psi, and **d** Au-AgNPs/macro-Psi hybrid structure

sample. The presence of Si element is owing to the Si substrate. As shown from this figure, the intensity of monometallic AuNP peak is lower than that of monometallic AgNPs and bimetallic Au-AgNPs, indicating higher deposition rate of AgNPs in both monometallic and bimetallic nanoparticles.

Electrical Characterization of Bare Macro-Psi Layer and Hybrid Structures

Figure 9a–d displays the *I–V* characteristics of the Al/macro-Psi/n-Si/Al, Al/AuNPs/macro-Psi/n-Si/Al, Al/AgNPs/macro-Psi/n-Si/Al, and Al/Au-AgNPs/macro-Psi/n-Si/Al hybrid

structures at room temperatures. The *I–V* characteristics of the Al/macro-Psi/n-Si/Al display as an ohmic contact behavior [21, 22]. After incorporation of bare macro-Psi layer with monometallic and bimetallic nanoparticles, this leads to enhance the rectification properties owing to the attendance of Schottky structure and the reducing resistivity of the macro-Psi layer [4]. These results point out that the barrier height of contact of bimetallic nanoparticle with the macro-Psi layer is higher than that of contact of monometallic nanoparticles with macro-Psi layer. The value of the barrier height ($\varnothing_{Bn}$) for n-type silicon is connected to the work function (Φ_{m}) and the electron affinity (χ) by the following relation [19]:

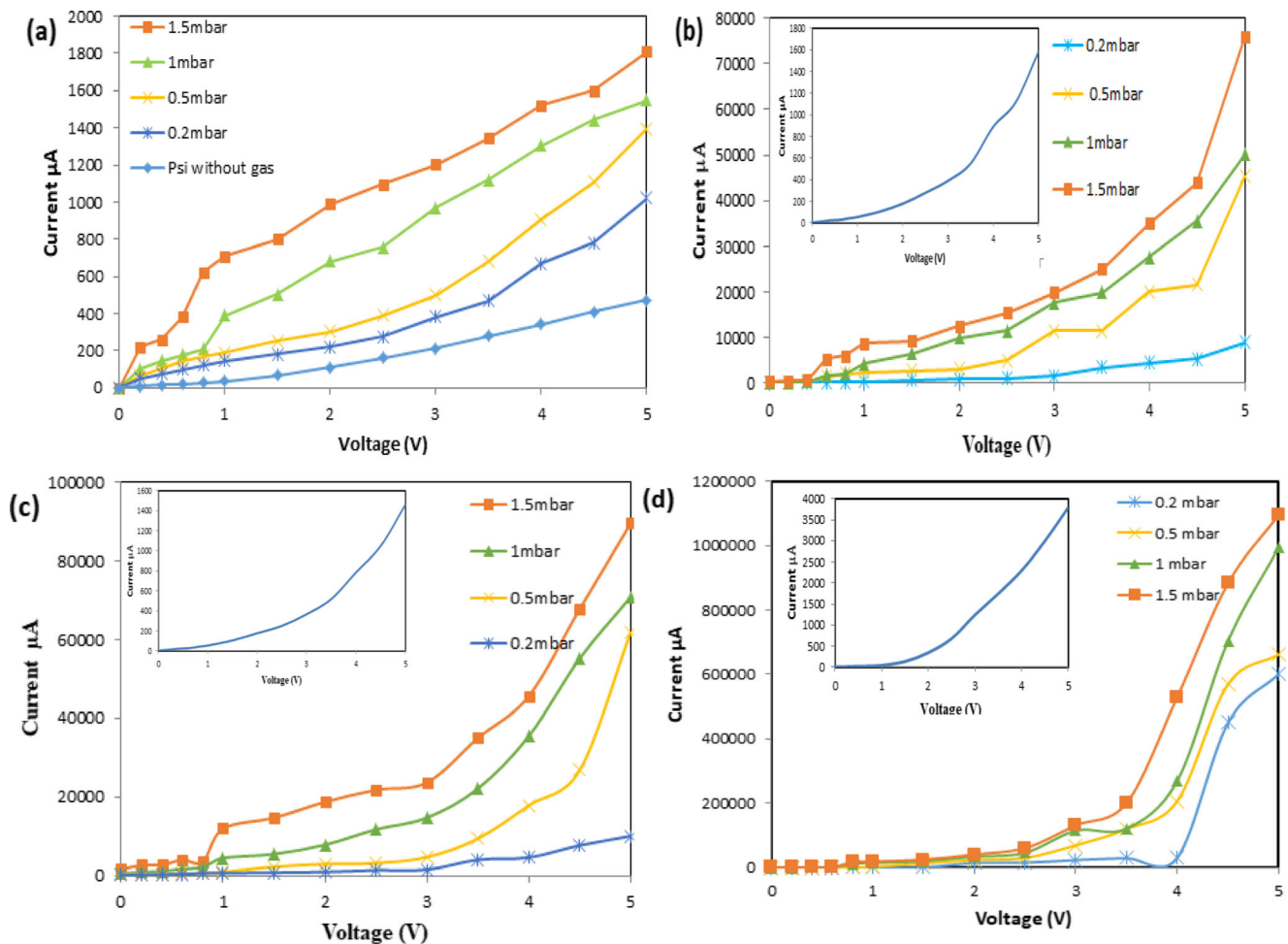$$\varnothing_{Bn} = \varnothing_m - \chi \tag{8}$$

Fig. 9 *I–V* characteristics of **a** Al/macro-Psi/n-Si/Al, **b** Al/AuNPs/macro-Psi/n-Si/Al, **c** Al/AgNPs/macro-Psi/n-Si/Al, and **d** Al/Au-AgNPs/macro-Psi/n-Si/Al hybrid structures at room temperatures; inset shows the *I–V* without gas

From Eq. 7, it can be inferred that the $\varnothing_{Bn}$ of bimetallic Au-AgNPs is higher than that of monometallic AuNPs and AgNPs [23]. Really, the values of $\varnothing_m$ of silver and gold are 4.26 and 5.1 eV, respectively [24]. The results in Fig. 9 show that the adsorption of CO_2 gas molecule has an important influence on the *I–V* characteristics of Al/macro-Psi/n-Si/Al, Al/AuNPs/macro-Psi/n-Si/Al, Al/AgNPs/macro-Psi/n-Si/Al, and Al/Au-AgNPs/macro-Psi/n-Si/Al hybrid structures. The incorporation of monometallic and bimetallic nanoparticles in bare macro-Psi layer increased the forward current after increasing the CO_2 gas at pressures in the range 0.2, 0.5, 1, and 1.5 mbar. For motivation of the electrical charge carrier trapping (initiating from adsorbate interaction with macro-Psi layers (dangling bond)), the Si-H states improve the conductance variations due to the trap/release of the charge carriers [19]. This difference is mainly related to desorption of the CO_2 molecules on the macro-Psi layer as a result of Vander Waals interaction [25]. The CO_2 desorption will change the relative permittivity of the macro-Psi layer.

The dependence of relative permittivity ϵr_{Psi} on the porosity of the macro-Psi layer and the gas (ϵ_{rgas}) is set by Eq. 9 [18, 26].

$$\varepsilon_{rpsi} = \varepsilon_{rsi} - P\% \left(\varepsilon_{rsi} - \varepsilon_{rgas} \right) \qquad (9)$$

where $P\%$ is the porosity of the bare macro-Psi layer and ϵ_{rgas} is the relative permittivity of the embedding medium (CO_2 molecule). Monometallic and bimetallic nanoparticles deposited on the walls of the macro-Psi layer act as a supplementary reason to increase the surface area and

Table 2 Barrier height of monometallic and bimetallic nanoparticles

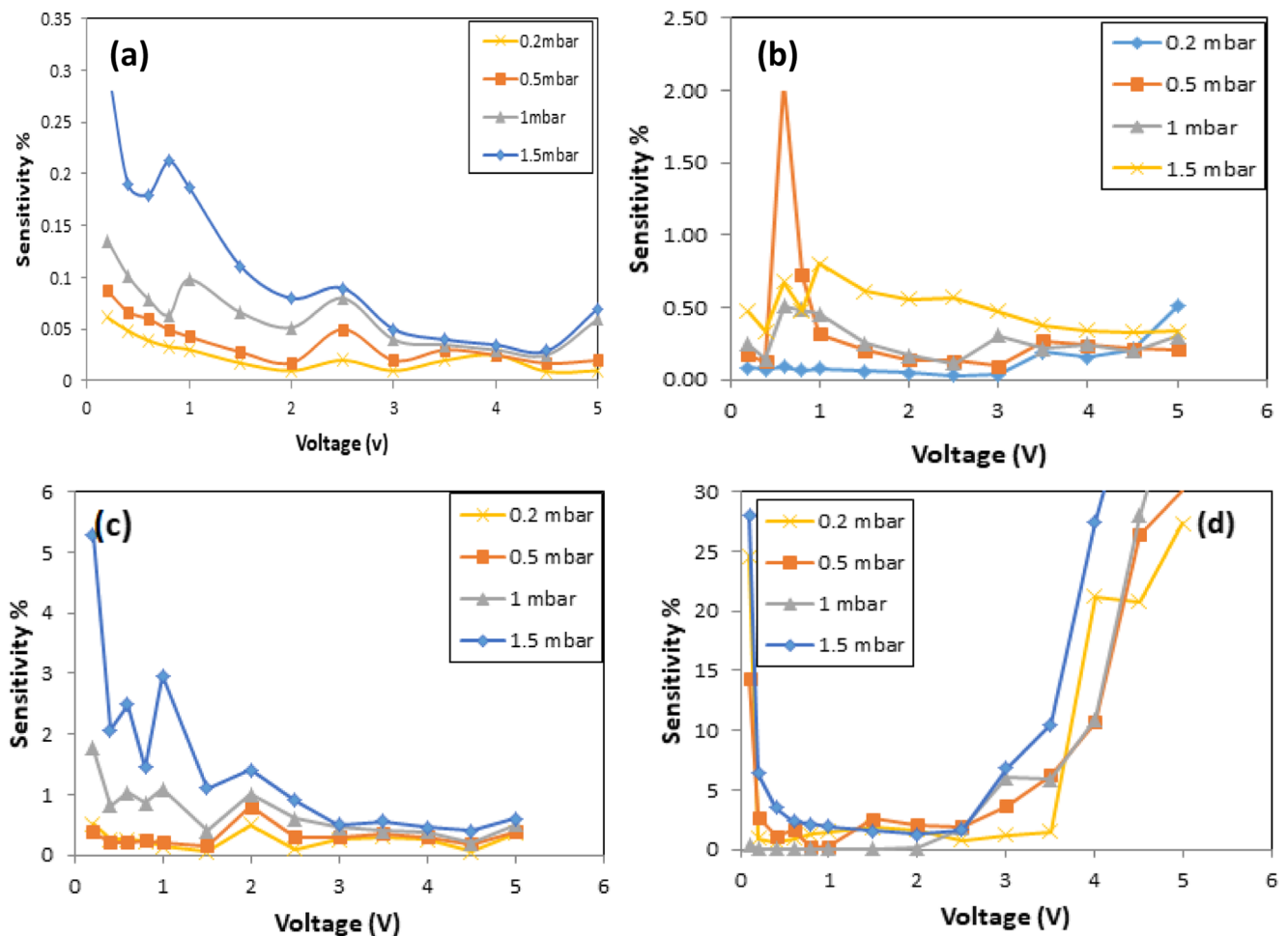| Hybrid structures	Barrier height (eV) exp.
AuNPs/macro-Psi	0.72
AgNPs/macro-Psi	0.7
Au-AgNPs/macro-Psi	0.82

Fig. 10 Sensitivity–voltage characteristics of **a** Al/macro-Psi/n-Si/Al, **b** Al/AuNPs/macro-Psi/n-Si/Al, **c** Al/AgNPs/macro-Psi/n-Si/Al, and **d** Al/Au-AgNPs/macro-Psi/n-Si/Al hybrid structures at room temperature

therefore improve the gas adsorption rate [4]. The bimetallic nanoparticles have higher SSA compared with monometallic nanoparticles. So the current increasing in the presence of the gas in bimetallic hybrid structure is much higher than that of monometallic hybrid structure. The sensitivity (S) of the sensor was calculated via the following formula [18, 27]:

$$S = \frac{Ig - Iv}{Iv} \qquad (10)$$

where I_g and I_v are the current in the existence and non-existence of CO_2 gas, correspondingly. Table 2 illustrates the barrier height of monometallic Au and Ag and bimetallic Au-Ag nanoparticles deposited on the bare macro-Psi layer. From this result, it is observed that Φ_{Bn} of bimetallic nanoparticles has a higher barrier height than that of monometallic.

Based on Table 2, it is observed that the results of the barrier height of monometallic (AuNPs/macro-Psi and AgNPs/macro-Psi) are in closer in agreement with the Bardeen model than the Schottky-Mott theory [28, 29], while the barrier height of bimetallic Au-AgNPs was in agreement with Arizumi et al. [23].

The sensitivity–voltage properties of the sensors allow defining the operated voltage range resultant to best sensitivity for different CO_2 gas pressures. Figure 10a–d displays the sensitivity vs. voltage characteristics of Al/macro-Psi/n-Si/Al, Al/AuNPs/macro-Psi/n-Si/Al, Al/AgNPs/macro-Psi/n-Si/Al, and Al/Au-AgNPs/macro-Psi/n-Si/Al hybrid structures under four CO_2 gas pressures at room temperature. The sensitivity of the structures grows with gas pressures. The highest sensitivity was achieved for the sensor of lowest metallic nanoparticle sizes (bimetallic Ag-AuNPs/macro-Psi hybrid structure) as compared with other bare macro-Psi layer and monometallic hybrid structures. The sensitivity of the Al/AgNPs/macro-Psi/n-Si/Al hybrid sensor is higher than Al/AuNPs/macro-Psi/n-Si/Al hybrid sensor; this variation in sensitivity is due to the higher deposition rate of AgNPs and hence high density compared with AuNPs. The highest
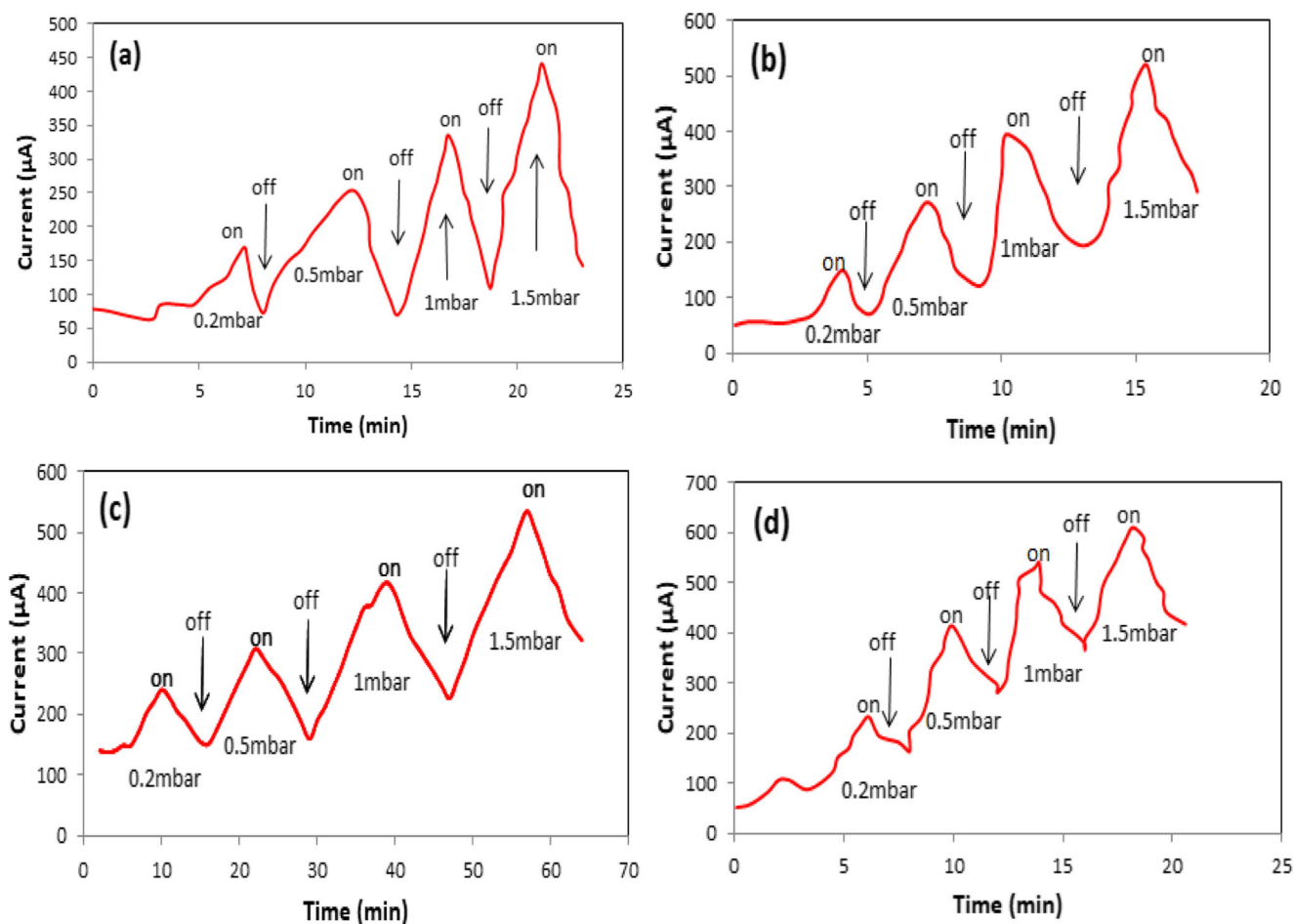
Fig. 11 Temporal response characteristics of **a** Al/macro-Psi/n-Si/Al, **b** Al/AuNPs/macro-Psi/n-Si/Al, **c** Al/AgNPs/macro-Psi/n-Si/Al, and **d** Al/Au-AgNPs/macro-Psi/n-Si/Al hybrid structures at room temperature

sensitivity of about 27% was achieved at a bias voltage of about 0.2 V for Al/Au-AgNPs/macro-Psi/n-Si/Al hybrid structure compared with 5.4% and 0.31% for Al/AgNPs/macro-Psi/n-Si/Al and Al/macro-Psi/n-Si/Al. The Al/AuNPs/macro-Psi/n-Si/Al hybrid sensor, the highest sensitivity of about 2.1%, was achieved at a bias voltage of about 0.6 V. This is attributed to the existence of Schottky barrier; the current is strong well ordered by the alteration in $\varnothing_{Bn}$, which is formed between the metallic nanoparticle layer and the macro-Psi

layer at low bias voltage, and controlled by specific surface area and the density of monometallic and bimetallic nanoparticles. From the current–voltage characteristics in the presence of gas molecules and the resulting barrier height, it is clear that the optimized response was achieved at structures with higher value of the barrier height.

Figure 11 shows the temporal response of the Al/macro-Psi/n-Si/Al, Al/AuNPs/macro-Psi/n-Si/Al, Al/AgNPs/macro-Psi/n-Si/Al, and Al/Au-AgNPs/macro-Psi/n-Si/Al hybrid

Table 3 Temporal response of the Al/macro-Psi/n-Si/Al, Al/AuNPs/macro-Psi/n-Si/Al, Al/AgNPs/macro-Psi/n-Si/Al, and Al/Au-AgNPs/macro-Psi/n-Si/Al hybrid structures at room temperature

	Concentration of CO_2							
	Response time (min)				Recovery time (min)			
	0.2 mbar	0.5 mbar	1 mbar	1.5 mbar	0.2 mbar	0.5 mbar	1 mbar	1.5 mbar
Al/macro-Psi/n-Si/Al	3.12	0.9	1.5	2.5	7.7	4.1	5	5.1
Al/AuNPs/macro-Psi/n-Si/Al	2.5	2	1.7	1.5	8	6	4.4	4
Al/AgNPs/macro-Psi/n-Si/Al	0.95	1	1.2	1.6	5	4.8	4	4.2
Al/Ag-AuNPs/macro-Psi/n-Si/Al	0.56	0.73	0.8	1	3.5	3	2	1.5

structures under four CO_2 gas pressures (0.2, 0.5, 1, and 1.5 mbar) at the optimum biasing applied voltage. This figure demonstrates that the response rises with the pressures of the gas for all sensors. Table 3 shows the temporal response values for all sensors. These values point out that they are lower for Al/Au-AgNPs/macro-Psi/n-Si/Al bimetallic sensor compared with other sensors (monometallic and bare macro-Psi layer). The significant short response and recovery times for Al/Au-AgNPs/macro-Psi/Al sensor may be because of the high rate of CO_2 gas adsorption and desorption.

Conclusion

We have effectively improved the room temperature macroporous silicon gas sensor performance by incorporating the macroporous silicon with bimetallic Au-Ag nanoparticles. Well-controlled simple immersion process of macro-Psi layer in $AgNO_3$ and $HAuCl_4$ solutions was employed to synthesize AuNPs/macro-Psi, AgNPs/macro-Psi, and Au-AgNPs/macro-Psi hybrid structure gas sensors. It has been noticed that the sensor performance depends greatly on the nanoparticle types and its size distribution. The highest sensitivity with minimum response and recovery times was achieved after depositing bimetallic compared with that of monometallic. The enhanced sensing properties of this sensor were attributed to the high value of integrated specific surface area of the bimetallic nanoparticles and the resulting Schottky barrier height.

References

1. Alwan AM, Naseef IA, Dheyab AB (2018) Well controlling of plasmonic features of gold nanoparticles on macroporous silicon substrate by HF acid concentration. Plasmonics 13(6):2037–2045
2. Martínez HM, Rincon NE, Torres J, Alfonso JE (2008) Porous silicon thin film as CO sensor. Microelectron J 39:1354–1355
3. Barillaro G, Nannini A, Pieri F (2003) A new, porous silicon-based gas sensing device. Sensors Actuators B 93:263–270
4. Naama S, Hadjersi T, Keffous A, Nezzal G (2015) CO2 gas sensor based on silicon nanowires modified with metal nanoparticles. Mater Sci Semicond Process 38:367–372
5. Ahmeda LB, Naamab S, Keffousb A, Hassein-Beya A, Hadjersi T (2015) H_2 sensing properties of modified silicon nanowires. Prog Nat Sci Mater Int 25:101–110
6. World Health Organization. Water, Sanitation and Health Team (2004) Guidelines for drinking-water quality. Recommendations, vol 1, 3rd edn. World Health Organization. http://www.who.int/iris/handle/10665/42852
7. Kumar M, Sandeep CSS, Kumar G, Mishra YK, Philip R, Reddy GB (2016) Plasmonic and nonlinear optical absorption properties of Ag:ZrO2 nanocomposite thin films. Plasmonics 11:261–267
8. Kumar M, Kumar T, Avasthi DK (2015) Study of thermal annealing induced plasmonic bleaching in Ag:TiO_2 nanocomposite thin films. Scr Mater 105:46–49
9. Kumar M, Reddy GB (2014) Stability-inspired entrapment of Ag nanoparticles in ZrO2 thin films. Plasmonics 9:129–136
10. Wilson SC, Jones KC (1993) Bioremediation of soil contaminated with polynuclear aromatic hydrocarbons (PAHs). Environ Pollut 81:229–249
11. Alwan AM, Hashim DA, Jawad MF (2018) Optimizing of porous silicon alloying process with bimetallic nanoparticles. Gold Bull 51:175–184
12. Wali LA, Hasan KK, Alwan AM (2019) Rapid and highly efficient detection of ultra-low concentration of penicillin G by gold nanoparticles/porous silicon SERS active substrate. Spectrochim Acta A Mol Biomol Spectrosc 206:31–36
13. Jabbar AA, Alwan AM, Haider AJ (2018) Modifying and fine controlling of silver nanoparticle nucleation sites and SERS performance by double silicon etching process. Plasmonics 13(4):1171–1182
14. Shin KS, Kim JH, Kim IH, Kim K (2012) Novel fabrication and catalytic application of poly (ethylenimin)-stabilized gold–silver alloy nanoparticles. J Nanopart Res 14:735
15. Liu X, Wang A, Yang X, Zhang T, Mou C-Y, Su D-S, Li J (2009) Synthesis of thermally stable and highly active bimetallic Au-Ag nanoparticles on inert supports. Chem Mater 21:410–418
16. Zhang Q, Lee JY, Yang J, Boothroyd C, Zhang J (2007) Size and composition tunable Ag–Au alloy nanoparticles by replacement reactions. Nanotechnology 18(245605):8
17. Zanoni R, Righini G, Mattogno G, Schirone L, Sotgiu G, Rallos F (1998) X-ray photoelectron spectroscopy characterization of stain-etched luminescent porous silicon films. J Lumin 80:159–162
18. Dheyab AB, Alwan AM, Zayer MQ (2018) Optimizing of gold nanoparticles on porous silicon morphologies for a sensitive carbon monoxide gas sensor device. Plasmonics 1–9. https://doi.org/10.1007/s11468-018-0828-x
19. Yang L, Li X, Tuo X, Van Nguyen TT, Luo X, Hong M (2011) Alloy nanoparticle plasmon resonance for enhancing broadband antireflection of laser-textured silicon surfaces. Opt Express 19(104):657–663
20. Sadr S, Azim-Araghi ME, Rahimi M, Dariani RS (2013) Effect of gold electrode annealing on gas sensing properties of nano-and microstructures of macroporous silicon. Indian J Pure Appl Phys 51:860–863
21. Alwan AM (2007) Calculation of energy band gap of porous silicon based on the carrier transport mechanisms. Eng Technol 25(10):1143–1148
22. Alwan AM, Abdulrazaq OA (2008) Aging effect on the photosynthesized porous silicon. Int J Mod Phys B 22(4):417–422
23. Arizumi T, Hirose M, Alitaf N (1967) Au-Ag alloy-silicon Schottky barriers. Jpn J Appl Phys 7(8):870
24. Shao M, Cheng L, Zhang X, Ma DDD, Lee ST (2009) Excellent photocatalysis of HF-treated silicon nanowires. J Am Chem Soc 131(49):17738–17739
25. Salameh S, van der Veen MA, Kappl M, van Ommen JR (2017) Contact forces between single metal oxide nanoparticles in gas-phase applications and processes. Langmuir 33(10):2477–2484
26. Sze SM (2008) Semiconductor devices: physics and technology. Wiley
27. Alwan AM, Dheyab AB (2017) Room temperature, CO_2 gas sensors of AuNPs/mesoPSi hybrid structures. Appl Nanosci 7(7):335–341
28. Verma S Kabiraj D Kumar T Kumar S, Kanjilal D (2010) Dependence of Schottky barrier height on metal work function. In: Proc AIP Conference Proceedings AIP, pp 1111–1112
29. Nienhaus H, Bergh HS, Gergen B, Majumdar A, Weinberg WH, McFarland EW (1999) Selective H atom sensors using ultra-thin Ag/Si Schottky diodes. Appl Phys Lett 74(26):4046–4048